

ENTIRE: Learning-based Volume Rendering Time Prediction

Zikai Yin*

Hamid Gadirov

Jiří Kosinka

Steffen Frey

University of Groningen

ABSTRACT

We present ENTIRE, a novel approach for volume rendering time prediction. Time-dependent volume data from simulations or experiments typically comprise complex deforming structures across hundreds or thousands of time steps, which in addition to the camera configuration has a significant impact on rendering performance. We first extract a feature vector from a volume that captures its structure that is relevant for rendering time performance. Then we combine this feature vector with further relevant parameters (e.g. camera setup), and with this perform the final prediction. Our experiments conducted on various datasets demonstrate that our model is capable of efficiently achieving high prediction accuracy with fast response rates. We showcase ENTIRE’s capability of enabling dynamic parameter adaptation for stable frame rates and load balancing in two case studies.

Index Terms: Rendering Time Prediction, Feature Extraction, Load Balancing, Scientific visualization

1 INTRODUCTION

Time-dependent volumes are typically collected from physical simulations or experiments, and generally contain volumes of high resolution in a collection of time steps conveying structures that are constantly moving and deforming. Direct volume rendering via raycasting is a powerful and widely employed approach for analyzing such data [4]. However, the performance of such algorithms depends heavily on parameter dimensions such as datasets, compute hardware, camera configurations, rendering techniques, and sampling rates [8]. As an example, Figure 1 shows one volume rendered from different camera poses and the corresponding rendering times.

The high computational demand when rendering high-resolution volumes with millions or even billions of cells in volume grid structures triggers challenges in different visualization use cases, from interactive exploration on workstations [4, 5] and clusters [39] to preparing image databases in in-situ visualization [1, 7]. Across these use cases, rendering performance prediction provides the basis to adjust the parameter settings of the rendering algorithm and/or task distribution, e.g., to achieve stable interactive frame rates or evenly balanced loads. According to a recent study [8], there are four factors that contribute to rendering time performance: hardware, rendering algorithm settings, camera parameter, and volume structure. All factors potentially have a significant effect on the final rendering time, and modeling the correlation of these factors is challenging [8].

In general, there are several application scenarios for rendering time prediction discussed in prior work, two of which are particularly prominent. First, this concerns the interactive exploration of time-dependent data. Here, performance prediction allows to support estimating how to adjust sampling parameters to yield stable

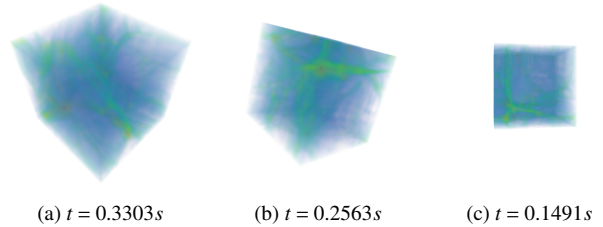


Figure 1: Rendering timings t from different camera poses via raycasting. The volume is the 1000th time step from the Nyx dataset.

rendering performance with the highest possible quality [5]. One use case is to adapt rendering parameters prior to generating a frame with the goal to meet a certain constraints, like a frame rate target. Second, in scenarios where rendering tasks are distributed across different compute hardware, the goal is to assign tasks so that the load is balanced (practically this typically means that optimally all nodes take the same amount of time to complete their tasks).

While there are prior works on predicting volume rendering timings [20, 6, 5, 39, 7], these models generally suffer from requiring significant manual modeling effort, low flexibility for adaption to other factors (rendering methods, graphics cards) or application scenarios, and are based on assumptions on the inner workings of the rendering methods. Larsen [20] developed an analytical model to evaluate rendering performance under explicit consideration of various cost factors (the parameters in the cost model require manual tuning). Bruder *et al.* [5, 6] focused on modeling the performance impact of early ray termination. Tkachev *et al.*’s model predicts rendering time based on hardware configurations for distributed volume raycasting [39]. For load balancing in in-situ visualization settings for creating Cinema-style image data bases, Bruder *et al.* [7] predict the rendering time of time-dependent dataset via probing (completing a subset of rendering tasks) and from this calculate the mean value of selected samples’ rendering times. On the one hand, this only yields a (predicted) average timing for each individual frame task, but no detailed information per frame to allow for higher-accuracy load balancing. On the other hand, considering more rendering tasks during probing increases prediction accuracy but increases cost and reduces the amount of work that can be flexibly distributed.

In this paper, we particularly address the question: *How to predict volume rendering time quickly and accurately (for dynamically changing time-dependent volumes)?*. Note that our approach generally works with any collection of volume data, but we consider scenarios with time-varying volume data to be the most relevant in practice. Among others, one influential factor impacting volume rendering performance is the volume itself, and it is of great importance for our rendering time prediction model to consider the volume’s key features that contribute to its rendering time performance. However, considering a full high-resolution volume with millions to billions of cells is time-consuming in itself for each prediction task. Therefore, to achieve high accuracy and efficiency, our model decouples the frame-time prediction procedure into two

*e-mail: zikai.yin@rug.nl

stages: (i) the generation of the feature vector from the volume (*VolumeNet*) and (ii) time prediction (*PredNet*). In short, we employ an autoencoder model [21] for learning a latent representation of the volume that can then further be used to generate accurate timing predictions. In this way, once a feature representation is extracted from a volume, timing predictions, e.g., considering various camera positions, can quickly be obtained with little cost (significantly faster than the actual rendering process).

In summary, we consider the main contributions of our work to be as follows:

- We present ENTIRE (rEnderiNg Time pREdiction network), a novel model (VolumeNet + PredNet) that decouples the extraction of volume features and the rendering time prediction.
- ENTIRE is generic in the sense that it does not rely on any assumptions regarding the rendering technique, data, or application scenario.
- We evaluate ENTIRE across various datasets and demonstrate its utility on several use cases.

To the best of our knowledge, our model is the first to achieve dynamic volume rendering time prediction using deep learning techniques. The source code will be released upon acceptance.

The remainder of the paper is organized as follows. We first review relevant related work (section 2), then present ENTIRE and its design (section 3), and follow this up with our experimental setup and architecture selection (section 4). We then evaluate ENTIRE’s rendering time prediction (section 5), discuss several use cases (section 6), and conclude the paper and present future research directions (section 7).

2 RELATED WORK

We start with reviewing state-of-the-art works in volume visualization (subsection 2.1), then we discuss relevant works in the directions of volume feature extraction (subsection 2.2) and rendering time prediction (subsection 2.3).

2.1 (Time-dependent) Volume Visualization

There are two different approaches for classical volume visualization, namely indirect volume rendering and direct volume rendering. The indirect method converts volume data to an intermediate representation (e.g., isosurface), while the direct method considers the data as a semi-transparent gel with physical properties and directly uses a 3D representation of it. Seminal works of indirect methods extracting isosurfaces are Marching Cubes [23] and Marching Tetrahedra [11]. For direct methods, the most prominently used approaches nowadays are based on raycasting [34] for rendering and early ray termination (ERT) for acceleration. The rendering time of raycasting-based algorithms is highly dependent on hardware and parameter setting. This provides a good evaluation scenario for ENTIRE; see below. Recently, further works have been proposed that focus on deep learning-based volume representations and rendering technique, called “Neural Rendering” [38]. In detail, neural rendering methods map a voxel to color and opacity using a neural network. However, training a neural rendering model usually requires significant computational resources and large datasets.

Our approach primarily focuses on visualizing volumes that are part of a larger collection, such as time series. In the context of visualizing time-dependent volumes, there are existing works that aim to reduce costs and enhance performance. Wang *et al.* [41] proposed to store data’s depth information to recover the evolution while reducing the sampling rate. Flexpath [10] reduces data movements and optimizes the data placements to save transfer costs. Frey *et al.* [13] introduced a method for time-step selection to reduce memory cost and speed up the rendering process. Gross *et al.* [15] proposed a sub-sampling algorithm of time-dependent data and further

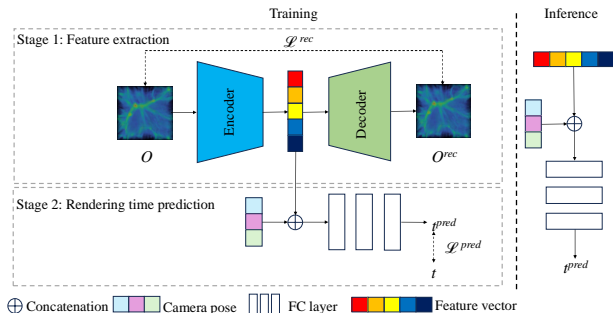


Figure 2: Overview of the proposed prediction model. Left: Model training. Right: Inference. \mathcal{L}^{rec} and $\mathcal{L}^{\text{pred}}$ are reconstruction loss and prediction loss, respectively (see subsection 3.5), and t^{pred} is the predicted rendering time. The details of VolumeNet and PredNet are illustrated in Figure 3 and Figure 4, respectively. We first train VolumeNet for collecting feature vectors. Then we train PredNet for rendering time prediction with collected feature vectors and camera poses.

processed the data on a local machine. This method focuses on assessing computation resource usage. Bruder *et al.* [7] adopted a hybrid in-situ method for generating Cinema databases efficiently. More specifically, they distribute rendering tasks between simulation nodes and visualization nodes dynamically based on a simple prediction model.

2.2 Volume Feature Extraction

Extracting a volume’s features and representing them properly has shown great importance in volume reconstruction and scene representation. Traditionally, a volume is represented via a large number of cells or points which explicitly store the volume and usually require a larger amount of memory. Recent works also consider that a volume can be stored by a neural network, i.e., using an implicit representation, including Occupancy Network [26], Scene Representation Networks [35], Neural Radiance Fields (NeRF) [27] as well as their variants [30, 45, 32, 44]. However, the required memory for storing the volume grows with the volume’s spatial resolution. Besides, the aforementioned algorithms can only represent static volumes or scenarios, and are not sufficient to represent deforming volumes in time-dependent datasets. Niemeyer *et al.* [28] introduced a network that learns time-dependent data by wrapping space and time, but the volume is still stored in the network’s weights. In contrast, we aim to have an explicit feature vector of the time-dependent dataset.

There are works [9, 25] which employ both explicit and implicit representation, where the neural network outputs a voxel grid that stores the volume’s feature. Unfortunately, such hybrid methods are designed for static scenarios and cannot represent dynamic time-dependent data properly. The output voxel grid is also still large and cannot cope with camera poses for rendering time prediction. Differently to this, our model utilizes time-dependent datasets as input to the network in order to adequately capture each volume’s structure. In doing so, each volume is represented as an explicit feature vector (as opposed to being stored via the network’s weights).

2.3 Rendering Time Prediction

The prediction and modeling of algorithm performance have evolved as important research topics in scientific visualization. With regard to predicting rendering time in volume rendering, several models that combine empirical measurements have been developed.

Sodhi *et al.* [36] created performance skeletons to model program execution times on the CPU. Ipek *et al.* [17] trained a neural

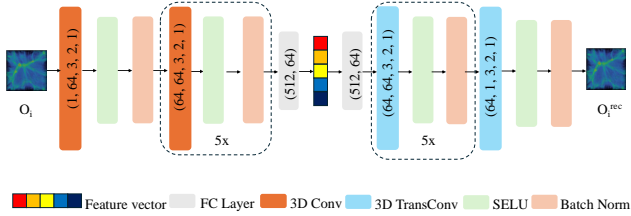


Figure 3: VolumeNet’s architecture. Here we assume the input of size 128^3 , and the feature vector dimension is 64. VolumeNet is a symmetric autoencoder. The encoder consists of six 3D convolutional blocks and one FC layer. Each 3D convolutional block includes a 3D convolutional layer, a batch normalization layer, and a SELU activation layer [19]. The decoder is symmetric to the encoder, except that all 3D convolutional layers are replaced with 3D transposed convolutional layers. The encoder compresses the input data into a feature vector, while the decoder reconstructs the data from this vector. For convolution layers, parameters are presented as *(input channel, output channel, kernel size, stride, padding)*. For transposed convolutional layers, parameters are presented as *(input channel, output channel, kernel size, stride, padding, output padding)*. For FC layers, we use *(input channel, output channel)*.

network to predict the performance of large-scale application running specifically on CPUs. These approaches are CPU architecture-specific, and thus inadequate for modeling rendering performance on GPUs. Bagsorkhi *et al.* [3] statically analyze GPU kernel code. Zhang and Owen [46] modeled GPU performance by conducting micro-benchmarks on the target platform. Lee *et al.* [22] proposed an early neural network-based approach that explicitly integrates statistical methods. Wu *et al.* [43] also applied machine learning to predict the scaling of power and time consumption of an application that scales with different GPU configurations. These above-mentioned methods primarily focus on offline applications, whereas we specifically target interactive volume visualization. Overall, there are fewer existing approaches that deal with performance prediction for real-time rendering compared to offline rendering.

Wimmer *et al.* [42] proposed a rendering time prediction framework that primarily focuses on modeling the contributions of CPUs and GPUs. Rizzi *et al.* [33] proposed an analytical model for GPU clusters’ scaling behavior for parallel rendering that explicitly accounts for and manually models each rendering stage. For in-situ visualization, Larsen *et al.* [20] modeled the performance of rasterization, ray tracing, and volume rendering analytically. They analyzed each application’s performance on a single machine and applied statistical methods to calculate the weights in their model. After that, they further extended the model to parallel execution by utilizing a similar model for evaluating image compositing performance. In contrast, our model can flexibly deal with different rendering methods, hardware, and tasks without manual adjustment.

Bruder *et al.* [5] further incorporated the effects of acceleration approaches (early ray termination and empty space skipping) and how this affects rendering time in interactive volume visualization. They then employed this for dynamically adjusting image resolution and load balancing. Tkachev *et al.* [39] predicted rendering time based on different hardware configurations. While they explicitly consider the inner workings of the (accelerated) raycasting method, their model implicitly learns the interplay of application and hardware, and users do not need to manually adapt the model to a given scenario. Bruder *et al.* [7] estimated time by rendering a random selection of images from poses of an arcball-style camera and using the arithmetic mean of the obtained times as the final time prediction. While this is agnostic to inner workings of methods and

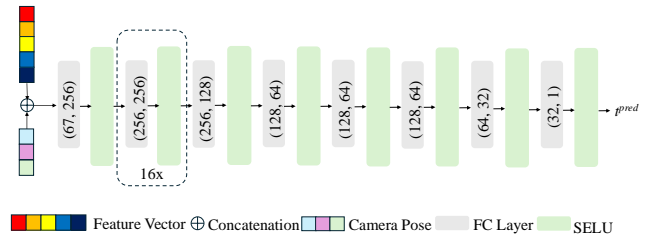


Figure 4: PredNet’s architecture. PredNet is a multi-layer perceptron (MLP). It takes the concatenated feature vector and camera pose as its input. Each FC layer’s output is projected by a SELU activation.

hardware, it requires many images to be actually rendered before being able to make a prediction, and it cannot accurately predict timings of individual frames. ENTIRE can adapt to complicated scenarios with heterogeneous render timings more quickly and accurately (see section 5 for a detailed discussion and evaluation).

3 Метод

We now describe ENTIRE in detail. In subsection 3.1, we first review relevant background on volume visualization and discuss the aspects that make timing predictions challenging in this context. After that, we introduce our two-stage model in subsection 3.2, whereas subsection 3.3 and subsection 3.4 describe both stages in detail. Finally, subsection 3.5 details the model’s loss functions.

3.1 Background

Volume rendering time is influenced by several factors, including hardware capabilities, rendering algorithm settings, camera parameters, and the structure as well as contents of the data. The final timing is a result of these factors, and modeling their correlation is in general challenging [8]. While we consider our model to be agnostic to the rendering technique, we limit ourselves to raycasting in the discussion and evaluation of this work as it has been the standard approach to volume rendering since the advent of (programmable) GPUs about two decades ago [37].

During the volume rendering process, as the ray travels through the volume, the volume’s scalar value at each sample s is mapped to color (r, g, b) and opacity O , specified by a transfer function and accumulated to yield the final pixel color. We further consider early ray termination: once the accumulated opacity on a ray reaches a pre-defined threshold (close to 1), the rendering procedure on this ray stops to save computation time. This means the rendering time is influenced by the contents of the volume (more precisely the opacity of each voxel). To reflect this, we transfer the scalar data to opacity O by applying the transfer function $f(\cdot)$ to volume V : $O = f(V)$. In other words, we consider classified volume data as input to ENTIRE.

3.2 Architecture Design

As illustrated in Figure 2, ENTIRE consists of two stages: feature vector extraction (VolumeNet) and rendering time prediction (PredNet).

VolumeNet (subsection 3.3). First, the model transforms the considered volume into a feature representation by using an autoencoder, which consists of two components: an encoder and a decoder. The encoder maps the data into a feature space, while the decoder reconstructs the data by remapping the feature space back to the original data space. In our implementation, the autoencoder leverages convolutional layers, transpose convolutional layers, and fully connected layers to enhance its feature representation capabilities (the decoder is only used for training purposes).

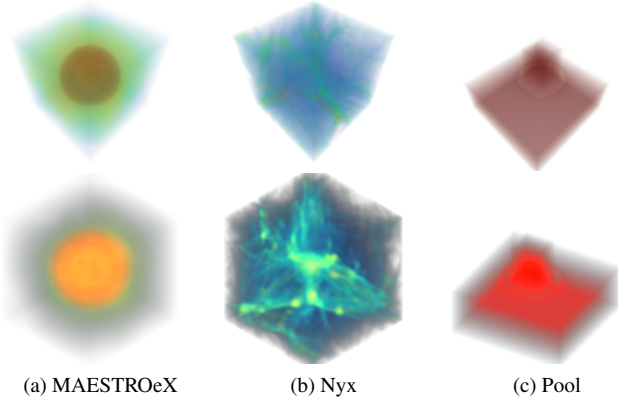


Figure 5: Datasets employed in this paper and their renderings with the CUDA raycaster (top) and yt (bottom).

Table 1: Dataset overview. The dimensions are reported as $M \times T \times W \times H \times D$, where M and T stand for the number of members and time steps, and W , H , D for the volume’s width, height, and depth.

Dataset	Dimension	Description
MAESTROeX	1×2000×512×512×512	White dwarf convection
Nyx	8×600×512×512×512	Dark matter’s N-body treatment
Pool	10×300×512×512×512	Water brick and pool collision

PredNet (subsection 3.4). At the prediction stage, the model combines the learned volume feature with camera poses (comprising position and orientation). The network consists of fully-connected layers only and finally outputs the final rendering time prediction.

The rationale underlying this two-stage design choice is that in many typical scenarios, several renderings are obtained from one volume by varying the camera position (e.g., as part of interactive exploration or by generating camera orbits for Cinema-style image databases [1]). The decoupling of the model into VolumeNet and PredNet means that in such cases the original volume only needs to be considered once, and from then onward for each change in camera only the much smaller feature representation of the volume needs to be taken into account.

3.3 VolumeNet: Feature Vector Extraction

At this stage, we extract a single feature vector from the volume using a neural network called VolumeNet (Volume feature extraction Network, see Figure 3). VolumeNet adopts an autoencoder architecture, where the encoder learns the volume’s feature representation, and the decoder reconstructs the volume from the learned feature. For time step i , where $i = 0, 1, \dots, n-1$, and X_i the feature vector of volume V_i , the encoder is formulated as

$$X_i = f_{\text{FC}}^1 \left(\bigodot_{u=1 \dots 5} \varphi^u \left(I_{\langle W_u, H_u, D_u \rangle} \right) \right), \quad (1)$$

where φ^u represents the u^{th} convolutional layer, and $I_{\langle W_u, H_u, D_u \rangle}$ denotes the input tensor to each layer with shape $\langle W_u, H_u, D_u \rangle$, where W , H , and D correspond to the width, height, and depth of the input volume, respectively. The function f_{FC}^1 is a fully connected (FC) layer that projects the output of the convolutional layers to the feature vector X_i .

The decoder’s objective is to recover the contents of the volume from the feature vector (for the sake of training the encoder). After a linear projection, the feature vector is reshaped into a 3D feature

map to match the input dimensions of the 3D transposed convolutional layer. The transposed convolutional layers then produce the final predicted scalar values.

In summary, the reconstructed volume opacity O_i^{rec} at time step i can be described as

$$O_i^{\text{rec}} = \bigodot_{v=1 \dots 5} \sigma^v \left(J_{\langle W_v, H_v, D_v \rangle} \right), \quad (2)$$

where σ is the v^{th} transposed convolutional layer, and J is the input of each layer with shape $\langle C_v, H_v, W_v \rangle$. The input $J_{\langle W_0, H_0, D_0 \rangle}$ of the transposed convolutional layers is

$$S_{\langle W_0, H_0, D_0 \rangle} = f_{\text{FC}}^2(X_i), \quad (3)$$

where $f_{\text{FC}}^2(\cdot)$ is the FC layer that projects X_i to the dimension that σ^v can process.

Figure 3 shows VolumeNet’s implementation details. The encoder in VolumeNet consists of several convolutional layers and a linear layer for linear projection. The VolumeNet decoder that is considered during training is symmetrical to the encoder, beginning with a linear layer followed by transposed convolutional layers.

3.4 PredNet: Rendering Time Prediction

The camera pose is captured in the vector η with the camera view always focused on the center of the volume; see subsection 4.1 for details.

Our rendering time prediction network PredNet is depicted in Figure 4. PredNet (denoted as $\psi(\cdot)$) consists exclusively of fully connected layers with non-linear activation functions. The input to the network is the concatenation of the dataset’s feature vector and the camera pose. Then, the predicted rendering time t_i^{pred} at time step i with regard to feature vector X_i and camera pose η is formulated as

$$t_i^{\text{pred}} = \psi(X_i, \eta). \quad (4)$$

3.5 Loss Functions

The reconstruction loss \mathcal{L}^{rec} for VolumeNet is calculated by measuring the voxel-wise difference between the ground-truth opacity O_i and its reconstructed counterpart O_i^{rec} . More specifically, the volume reconstruction loss is defined as the voxel-wise mean square error between O_i and O_i^{rec} , i.e.,

$$\mathcal{L}^{\text{rec}} = \frac{1}{n} \sum_{i=0}^{n-1} \|O_i - O_i^{\text{rec}}\|_2^2. \quad (5)$$

Since the task of predicting rendering time is inherently a regression problem, the mean squared error (MSE) serves as the most straightforward and effective loss function.

This is also the case with the objective of minimizing the difference between predicted and actual rendering times with PredNet. With t_k representing the ground-truth rendering time, the prediction loss is formulated as:

$$\mathcal{L}^{\text{pred}} = \frac{1}{n} \sum_{i=0}^{n-1} \|t_i - t_i^{\text{pred}}\|_2^2. \quad (6)$$

\mathcal{L}^{rec} and $\mathcal{L}^{\text{pred}}$ are applied independently in the training process of Stage 1 and Stage 2, respectively (subsection 3.2).

4 EXPERIMENTAL SETUP AND ARCHITECTURE SELECTION

We now describe the datasets used and parameter settings (subsection 4.1), followed by concrete architecture choices (subsection 4.2).

Table 2: Prediction MSE values (in $\times 10^{-5}$ for CUDA raycaster, $\times 10^0$ for yt), inference time of VolumeNet ($T_{\text{infer}}^{\text{vol}}$) & PredNet ($T_{\text{infer}}^{\text{pred}}$) for different volume resolution and feature vector dimension F . Inference times are in milliseconds; best prediction results are highlighted in bold.

Framework	Dataset	Resolution	MSE / $T_{\text{infer}}^{\text{vol}} \downarrow / T_{\text{infer}}^{\text{pred}} \downarrow$				
			F = 16	F = 32	F = 64	F = 128	F = 256
CUDA raycaster	MAESTROeX	64 × 64 × 64	1.895 /2.226/0.143	194.3/1.777/0.148	197.2/0.621/0.142	2.062/1.620/0.147	1.949/1.647/0.146
		128 × 128 × 128	1.946/1.758/0.141	2.049/2.016/0.140	1.944/0.673/0.141	1.968/0.531/0.143	1.984/0.555/0.141
	Nyx	64 × 64 × 64	1.345/1.435/0.141	1.404/1.589/0.144	1.359/0.728/0.145	1.414/1.945/0.140	1.304/1.589/0.139
		128 × 128 × 128	1.387/1.853/0.141	1.291 /1.544/0.145	1.307/2.554/0.140	1.368/2.305/0.145	1.319/0.844/0.147
	Pool	64 × 64 × 64	2.095/3.768/0.135	2.128/3.115/0.140	2.350/0.466/0.135	2.315/1.519/0.133	2.384/1.528/0.136
		128 × 128 × 128	2.034 /1.781/0.143	2.227/2.142/0.142	2.249/1.245/0.144	2.181/1.758/0.144	2.426/2.215/0.142
yt	MAESTROeX	64 × 64 × 64	9.150/3.417/0.149	874.8/2.214/0.142	854.3/2.271/0.140	844.1/3.613/0.140	848.3/2.179/0.141
		128 × 128 × 128	9.125/3.591/0.151	873.6/3.593/0.149	856.5/3.398/0.146	847.4/3.241/0.142	843.0 /1.399/0.141
	Nyx	64 × 64 × 64	9.872 /1.972/0.142	10.05/1.483/0.142	10.29/0.973/0.146	10.76/1.513/0.140	10.91/1.469/0.142
		128 × 128 × 128	10.10/2.996/0.149	10.33/1.902/0.149	10.38/1.445/0.139	10.49/2.159/0.145	11.03/1.886/0.142
	Pool	64 × 64 × 64	2.999/2.996/0.142	3.104/1.536/0.151	3.462/0.935/0.142	3.417/0.347/0.140	3.461/4.404/0.145
		128 × 128 × 128	2.938 /2.301/0.142	2.989/0.446/0.141	3.365/0.527/0.152	3.520/0.682/0.145	3.825/0.424/0.140

4.1 Experimental Setup

Datasets. The three datasets we employed in this paper are listed in Table 1. For the interactive exploration of time-dependent data, we use MAESTROeX [12]. MAESTROeX simulates low Mach number stratified flows. More specifically, we selected the white dwarf convection problem in MAESTROeX as our dataset.

For distributed visualization, we use Nyx [2] and the Pool dataset. Nyx is a cosmological simulation developed by Lawrence Berkeley National Laboratory. It simulates the evolution of baryonic gas coupled with an N-body treatment of the dark matter. The Pool dataset is a self-generated CFD dataset and simulates a scenario where a water brick drops into a pool. To save memory space, we converted all three dataset from their original format to ubyte files by normalizing the raw data to [0, 255]. Then, we applied our transfer function $f(\cdot)$ to the converted volumes to obtain opacity. All opacity values were normalized to $[-1, 1]$ before serving as input to ENTIRE.

For MAESTROeX, 2000 volumes were randomly divided into 1600 for training, 200 for validation, and 200 for evaluation. We used 6 members from Nyx for training, 1 member for validation, and 1 member for evaluation. For Pool, 8 members were used for training, 1 member for validation, and 1 member for evaluation. Figure 5 presents the datasets used in this study, rendered by CUDA raycaster and yt [40]. The latter is an advanced rendering framework implemented in Python and limited to CPU rendering. (Please note that the gray areas in the yt renderings are due to a bug in the framework; the issues has been reported but has not yet been resolved at the time of writing.)

To evaluate ENTIRE’s generalizability across GPU and CPU platforms, we utilized a CUDA volume raycaster running on the GPU [29] and yt (executed on the CPU). In our experiments with the CUDA code, the threshold for early ray termination was set to its default value of 0.99. Additionally, we implemented local lighting and used central difference for gradient calculations. The CUDA raycaster was run on desktop machine with an NVIDIA RTX 3060 GPU, and for yt we used a node of a compute cluster equipped with an AMD 7763 CPU (32 threads). Note that yt took roughly 100× longer on average when compared to the CUDA raycaster for a similar volume.

Data collection. Bruder *et al.* [8] highlighted that data sampled from a camera in an arcball-style orbit provides good coverage of rendering time distributions. We followed a similar strategy. Our camera followed the surfaces of several semi-spheres with various radii, expressed using spherical coordinates and stored in η . To ensure stable time measurements, each frame was rendered multiple times, and the median rendering time was taken as the final value. Each volume was rendered 100 times from random poses to collect training data. For validation and evaluation sets, each volume was

rendered 10 times from random poses.

Training parameter setting. We employed the Adam optimizer [18] and trained our model using the cosine annealing learning rate decay strategy [24]. Adam’s momentum settings are $\beta_1 = 0.9, \beta_2 = 0.999$. To prevent overfitting, early stopping was applied to halt the training process once the validation loss ceased to decrease. Additionally, we applied gradient clipping with a maximum norm of 1.0 to avoid gradient explosion. VolumeNet was trained for 150 epochs and evaluated on a single Nvidia A100 GPU, with batch size of 16 and decreasing learning rate in range $[10^{-3}, 10^{-5}]$. PredNet was trained for 200 epochs and tested on a Nvidia RTX 3060 GPU. For the CUDA raycaster, we set PredNet’s decreasing learning rate to $[10^{-4}, 10^{-6}]$. As for yt, the decreasing learning rates were set to $[5 \times 10^{-5}, 5 \times 10^{-7}]$, $[5 \times 10^{-6}, 5 \times 10^{-8}]$, and $[5 \times 10^{-7}, 5 \times 10^{-9}]$ for MAESTROeX, Nyx, and Pool, respectively. Training VolumeNet required approximately 0.5 hours for 64^3 volumes and 2.5 hours for 128^3 volumes over 150 epochs. In contrast, training PredNet took only a few minutes.

Baseline. We adopted another generic rendering time prediction method as our baseline model, the approach recently used by Bruder *et al.* [7]. As discussed in subsection 2.3, while there are several models that rely on manual modeling and consider specifics of the rendering approach and the compute hardware, ENTIRE has been designed to be agnostic to these factors. We therefore chose this model by Bruder *et al.* as it also can be employed across methods and compute architectures without requiring manual adaptation. In this baseline, as specified by the authors of the method, 15% of rendering jobs are selected from a set of rendering tasks, and the final rendering time estimate is then calculated as the arithmetic mean of the sampled rendering times.

Evaluation setup. To evaluate ENTIRE’s prediction accuracy, we used the mean square error (MSE) as our evaluation metric. In addition to accuracy, we also measured the time ENTIRE required during both the training and inference phases. It is important to note that for VolumeNet, we did not compare its reconstruction quality as we are rather interested in how well the features support the subsequent prediction task.

4.2 Architecture Selection

We now describe how we selected the final ENTIRE architecture. Below, we refer to architecture variants in short form, such as $128^3\text{F16} \rightarrow 5\text{C256}$:

F is used to indicate the resolution of the input volume and the dimensionality of the volume feature vector. For instance, 128^3F16 indicates a volume of dimension 128^3 encoded into a feature vector of length 16.

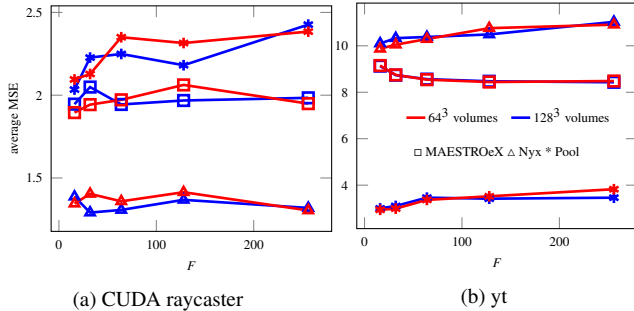


Figure 6: Comparison of average MSE values (in $\times 10^{-5}$ for CUDA raycaster and $\times 10^0$ for yt) of different volume resolution and feature vector dimension.

Table 3: Further investigation of feature vector dimension. The average MSE is displayed in $\times 10^{-5}$ for CUDA raycaster and $\times 10^0$ for yt. The inference time is displayed in milliseconds. We highlighted the best prediction results in bold font.

Framework	Dataset	Model	MSE \downarrow / T_{infer}^{vol} / T_{infer}^{pred}
CUDA raycaster	MAESTROeX	$64^3 F8 \rightarrow 4C256$	1.917/3.798/0.138
		$64^3 F16 \rightarrow 4C512$	1.896 /2.226/0.144
	Pool	$128^3 F8 \rightarrow 4C256$	2.062/2.270/0.145
		$128^3 F16 \rightarrow 4C256$	2.034/1.781/0.144
	MAESTROeX	$128^3 F256 \rightarrow 4C256$	8.430 /1.399/0.141
		$128^3 F512 \rightarrow 4C256$	8.500/2.380/0.140
yt	Nyx	$64^3 F8 \rightarrow 4C256$	10.20/3.762/0.144
		$64^3 F16 \rightarrow 4C256$	9.872 /1.972/0.142
	Pool	$128^3 F4 \rightarrow 4C256$	2.932/2.753/0.137
		$128^3 F8 \rightarrow 4C256$	2.912 /2.780/0.140
	Pool	$128^3 F16 \rightarrow 4C256$	2.938/2.301/0.142

C depicts fully-connected layers. It is preceded by the number of layers, and followed by the number of channels of the first layer; the number of channels repeats for each following layer. For instance, 16C256 denotes 16 repeated fully-connected layers, with the input and output size of 256; see Figure 4. Note that PredNet’s rest layers are not explicitly represented in this notation. Each layer’s dimension is halved with respect to its previous layer.

→ denotes the transition between a feature vector and fully-connected layers.

Accordingly, $128^3 F16 \rightarrow 5C256$ means that VolumeNet considers volumes with a resolution of 128^3 and the output feature vector’s dimension is 16. The corresponding PredNet has 5 fully-connected layers as described above.

Our architecture selection has three steps and is mainly focused on three architectural factors that influence the final prediction accuracy: (1) the resolution of the volume as input to VolumeNet, (2) the dimensionality of the feature vector describing the volume (output of VolumeNet, input to PredNet), and (3) the number of C256 layers in PredNet. We aim for a model that works well across all datasets and rendering frameworks. Accordingly, we tested selected models on every ‘rendering framework + dataset’ scenario and calculated the relative deviation to the lowest prediction error. We finally select the model with the lowest mean relative deviation (MRD) is the final model.

(1) **Volume resolution.** We tested with volume resolutions 64^3 and 128^3 . Training VolumeNet on volumes with higher resolutions cost more than 15 hours, which is not practicable in our target application scenarios. Note that all volumes for training and testing here were downsampled from the original full volumes, and that this downsampling only applies to VolumeNet input. The rendering time measurements used to train PredNet are captured with the

Table 4: Comparison of average MSE (in $\times 10^{-5}$ for CUDA raycaster and $\times 10^0$ for yt) of different PredNet architectures and inference time T_{infer}^{pred} (in milliseconds per pose). Best predictions are in bold.

Framework	PredNet	MSE \downarrow / T_{infer}^{pred}			
		MAESTROeX	Nyx	Pool	
CUDA raycaster	22C256	1.793/0.378	1.243/0.359	1.934/0.373	
	20C256	1.838/0.349	1.247/0.336	1.899/0.339	
	18C256	1.804/0.317	1.322/0.321	1.914/0.321	
	16C256	1.825/0.286	1.244/0.301	1.851 /0.301	
	14C256	1.759/0.274	1.241 /0.266	1.996/0.270	
	12C256	1.746/0.237	1.297/0.253	1.867/0.253	
	10C256	1.806/0.214	1.275/0.221	1.924/0.222	
	8C256	1.856/0.193	1.291/0.199	1.952/0.203	
	6C256	1.937/0.167	1.261/0.173	2.030/0.175	
	4C256	1.896/0.142	1.291/0.150	2.034/0.143	
	2C256	2.126/0.115	1.328/0.119	2.341/0.122	
	0C256	3.418/0.093	1.828/0.097	3.794/0.093	
	yt	38C256	-	-	2.356/0.550
		36C256	-	-	2.272/0.536
34C256		-	-	2.322/0.500	
32C256		-	-	2.381/0.471	
30C256		-	-	2.204 /0.455	
28C256		-	-	2.366/0.431	
26C256		-	-	2.410/0.405	
24C256		-	-	2.209/0.394	
22C256		-	9.622/0.381	2.238/0.360	
20C256		-	9.438/0.351	2.222/0.333	
18C256		8.652/0.313	9.743/0.318	2.277/0.310	
16C256		8.466/0.291	9.592/0.298	2.298/0.285	
14C256		8.673/0.268	9.504/0.264	2.382/0.261	
12C256		8.470/0.242	9.434 /0.255	2.594/0.240	
10C256	8.443/0.216	9.520/0.216	2.593/0.212		
8C256	8.440/0.191	9.768/0.196	2.937/0.197		
6C256	8.463/0.167	9.684/0.174	2.992/0.168		
4C256	8.430 /0.141	9.872/0.146	2.912/0.140		
2C256	8.511/0.121	10.83/0.118	3.093/0.115		
0C256	8.995/0.097	11.62/0.096	3.667/0.090		

original volume size. We experimented with five different feature vector sizes {16, 32, 64, 128, 256} and four C256 layers.

Interestingly, a higher input volume resolution to VolumeNet does not necessarily lead to a higher prediction accuracy. Table 2 indicates for the CUDA raycaster that ENTIRE showed its best performance with 64^3 for MAESTROeX and 128^3 for Nyx and Pool. For yt, the best performance was achieved with 128^3 for MAESTROeX and Pool, and 64^3 for Nyx. From Table 2, we conclude that the prediction accuracy is co-affected by both volume resolution and feature vector dimension. If the input volume resolution is large while the feature vector dimension is low, then the feature vector is not be able to fully include all useful volume features, lowering prediction accuracy. Higher input resolution also substantially increases training costs, resulting in 5-fold increase for 128^3 .

(2) **Feature vector dimension.** From Table 2, we see that for the CUDA raycaster, ENTIRE’s best volume resolution and feature vector dimension combinations are $64^3 F16$, $128^3 F32$, and $128^3 F16$ for MAESTROeX, Nyx, and Pool, respectively. For yt, the best combinations are $128^3 F256$, $64^3 F16$, and $128^3 F16$. For both the CUDA raycaster and yt, the best performance was achieved with F16 and F256, which are the lower and upper limit, respectively, of feature vector dimension settings in Table 2. Therefore, we visualized Table 2 in Figure 6 to gain further insights. For the rendering time prediction task on MAESTROeX, the overall trend is that the larger the feature vector dimension, the higher the prediction accuracy, both for the CUDA raycaster and yt (Figure 6). For the rendering time prediction task on Nyx and Pool, however, ENTIRE showed different behaviour across the renderers.

When the CUDA raycaster was employed, as F grew, the prediction accuracy fluctuated on Nyx and Pool. On the one hand, if F is too low, it fails to adequately encode the volume features. On the other hand, if F is too high, the contribution of the camera pose is diminished in PredNet’s input. Consequently, the model does not fully account for the impact of camera poses, resulting in reduced prediction accuracy. Since Nyx contains more data points and has more complicated shapes, it makes sense that Nyx requires the feature vector of a higher dimension for precise prediction. As for Pool, since its inner structure is relatively simple, F16 produces

Table 5: Comparison of average MSE of different PredNet architectures, inference time (in ms per each pose), and relative deviation. They are separated by “/”. For all dataset, the average MSE are displayed in $\times 10^{-5}$ for CUDA raycaster and $\times 10^0$ for yt. “*” indicates that the results were from the baseline model. “RD” is relative deviation and “MRD” is each model’s mean value of relative deviations. We highlighted the best prediction accuracy and MRD in bold font.

Framework	Dataset	$MSE \downarrow / T_{infer}^{vol} \downarrow / T_{infer}^{pred} \downarrow / RD \downarrow$				
		$64^3F16 \rightarrow 12C256$	$128^3F8 \rightarrow 30C256$	$128^3F16 \rightarrow 16C256$	$128^3F32 \rightarrow 14C256$	$128^3F256 \rightarrow 5C256$
CUDA raycaster	MAESTROeX	1.746*/2.226/0.237/8.50%	1.609 /2.201/0.452/0%	1.807/1.758/0.289/12.30%	1.837/2.016/0.271/14.12%	1.984/0.555/0.141/23.29%
	Nyx	1.293/1.435/0.256/4.20%	1.324/2.223/0.483/6.69%	1.317/1.853/0.285/6.12%	1.241* /1.544/0.266/0%	1.319/0.844/0.147/6/27%
	Pool	1.820 /3.768/0.239/0%	1.979/2.270/0.463/8.71%	1.852*/1.781/0.293/1.74%	1.934/2.142/0.261/6.30%	2.426/2.215/0.142/33.27%
yt	MAESTROeX	8.662/3.417/0.228/2.75%	9.315/2.380/0.455/10.50%	8.748/3.591/0.296/3.77%	8.718/3.593/0.263/3.42%	8.430* /1.399/0.141/0
	Nyx	9.434* /1.972/0.255/0%	9.849/1.814/0.464/4.40%	9.581/1.926/0.294/1.56%	10.05/1.902/0.264/6.56%	11.02/1.886/0.142/16.90%
	Pool	2.490/2.996/0.239/13.19%	2.204*/2.799/0.431/1.78%	2.200 /2.301/0.291/0%	2.633/0.446/0.177/19.69%	3.825/0.424/0.140/73.91%
MRD		4.77%	5.07%	4.24%	8.34%	25.61%

acceptable accuracy.

When yt was employed, the final prediction accuracy decreased as F grew for both Nyx and yt. To further explore the feature vector dimension’s effect on prediction accuracy, we took the models from Table 2 which have the best performance and used them as the baseline model. If F in the baseline model is 16, then we decreased it until ENTIRE’s prediction accuracy showed a downward trend. Similarly, we increase F from 256 until ENTIRE’s prediction accuracy stopped growing. The results are presented in Table 3.

Overall, the best input volume size and feature vector dimension for the CUDA raycaster are 64^3F16 , 128^3F32 , and 128^3F16 for MAESTROeX, Nyx, and Pool. For yt, the best input volume size and feature vector dimension are 128^3F256 , 64^3F16 , and 128^3F8 .

(3) PredNet architecture selection. We now aim to determine a good balance between the final prediction accuracy and PredNet’s inference speed by considering the number of $C256$ layers in PredNet. We started with a maximum of eight layers, and continued increasing the count until PredNet stopped improving (see Table 4). For all three datasets, the overall trend is that as PredNet gets deeper, the prediction accuracy increases and reaches its peak. Then, the prediction accuracy of PredNet stopped increasing and started to decline due to overfitting. For the CUDA raycaster, the optimal ENTIRE architectures are $64^3F16 \rightarrow 12C256$, $128^3F32 \rightarrow 14C256$, and $128^3F16 \rightarrow 16C256$ for MAESTROeX, Nyx, and Pool. For yt, the optimal ENTIRE architectures are $128^3F256 \rightarrow 4C256$, $64^3F16 \rightarrow 12C256$, and $128^3F8 \rightarrow 30C256$ for MAESTROeX, Nyx, and Pool. As expected, the model with the least number of layers has the fastest inference speed.

Final model selection. We have six “optimal” models in total (one for each dataset \times renderer pair). To select one model that performs well across all scenarios and datasets, we trained these six model architectures for both the CUDA raycaster and yt rendering scenarios across on all datasets. Then, we compared the prediction accuracy of each model with the best performance by calculating relative deviations. The model with the lowest mean relative deviation was selected as our final model. As shown in Table 5, the optimal model is $128^3F16 \rightarrow 16C256$. We also noticed that some of these models surpassed the baseline model in terms of prediction accuracy, i.e., it benefits from training with a larger variety of volumes. For example, the baseline model for ‘CUDA raycaster + Pool’ is $128^3F16 \rightarrow 16C256$ while the best performance was given by $64^3F16 \rightarrow 12C256$. Our model architecture selection procedure yields a model with high prediction accuracy, but also other model configurations can yield comparable performance. Overall, it shows that good performance can be achieved across a range of considered model configurations, also for scenarios which have not explicitly been considered in the selection process.

Algorithm 1: Steering ray step size. In our evaluation, we consider a camera *path* with a duration of T .

```

Input: path,  $T$ ,  $t^{\text{target}}$ ,  $G$ , ENTIRE, volume
1 timer.start();
2 while timer <  $T$  do
3   pose = path(timer);
4    $t^{\text{predict}}$  = ENTIRE(volume, pose);
5    $\delta^{\text{adapt}}$  =  $\delta^{\text{ref}} G^{-1} \left( \frac{t^{\text{target}}}{t^{\text{predict}}} \right)$ ;
6   renderer(volume, pose,  $\delta^{\text{adapt}}$ );
7 end

```

5 EVALUATION OF RENDERING TIME PREDICTION

Table 6 presents prediction accuracy and runtime across different datasets and compares ENTIRE to the baseline [7]. We use MSE to assess prediction accuracy, and the average time per prediction (in milliseconds) quantifies the inference speed of ENTIRE. Detailed results can further be seen via the camera paths in Figure 7, Figure 8, and Figure 9. The baseline collects timings from a random subset (15%) of considered datasets and poses, using the mean value as (constant) prediction (in Table 6 we report the time it took to collect timings from this subset—there is no induced prediction cost afterwards).

ENTIRE exhibits high prediction accuracy with fast inference speed overall. The comparison with the baseline model shows that with ENTIRE the MSE of the rendering time prediction is lower by almost two orders of magnitude across all cases. Notably, ENTIRE’s inference both concerning VolumeNet and PredNet induces only a small computational footprint: $T_{infer}^{vol} < 4$ ms and $T_{infer}^{pred} < 0.3$ ms, respectively. With this, they are substantially faster than generating an image using either renderer (avgRT in Table 6). Still, in scenarios where fast inference speed is crucial, we see the advantages of our two-stage model as VolumeNet only needs to run only once per volume and can be reused for different camera poses. Overall, these results demonstrate that ENTIRE is highly efficient in predicting rendering times with high precision.

A more detailed look into prediction timings by means of Figure 7, Figure 8 and Figure 9 further shows that ENTIRE delivers accurate predictions across various time steps, demonstrating that VolumeNet successfully captures the key features of different volumes. While ENTIRE achieves almost perfect prediction results for the CUDA raycaster, the deviations with yt are slightly larger. We partially attribute this to the fact that the CUDA raycaster used in this paper is a standard implementation of front-to-back volume raycasting with early ray termination, whereas the rendering process with yt is more complex and predicting its rendering tim-

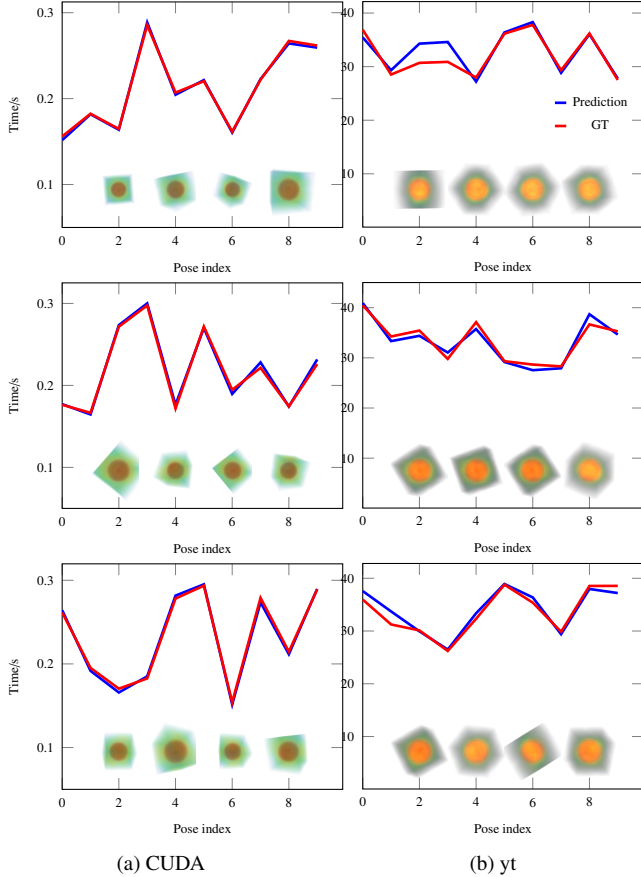


Figure 7: Rendering time prediction of ENTIRE for MAESTROeX. GT stands for ground-truth (measured) time. Here we selected three representative results for early (517), middle (1023), and later (1532) time steps from the time series (from top to bottom). At the bottom of each figure are the rendered volumes from a specific (indexed) camera pose. The left column depicts results for the CUDA raycaster, the right column shows results for yt.

ing behavior is more challenging. We also observed some outliers with unusually high rendering times in our measured yt timings for MAESTROeX and Nyx—the two datasets with the largest prediction errors with yt—which we anticipate also had an impact on the performance of the trained model. Only 0.05% and 0.075% of images take more than a minute to render for the two data sets, respectively; when we omit them from MSE calculation the prediction error drops to 5.752 for Nyx and 2.287 for MAESTROeX. Despite these outliers, ENTIRE still successfully captures the trends in yt’s rendering timing, producing predictions with small errors only.

In sum, our experiments demonstrate that ENTIRE robustly delivers high accuracy and fast inference speeds for different raycasting methods and across GPU and CPU environments.

6 USE CASES

We now discuss two use cases of ENTIRE: ray step size control (subsection 6.1) and load balancing (subsection 6.2).

6.1 Steering Ray Step Size of Stable Frame Rates

Achieving interactive frame rates reliably is essential to enable fluent exploration for many visualization tasks. In this use case, our goal is to render frames while not exceeding a certain timing bound

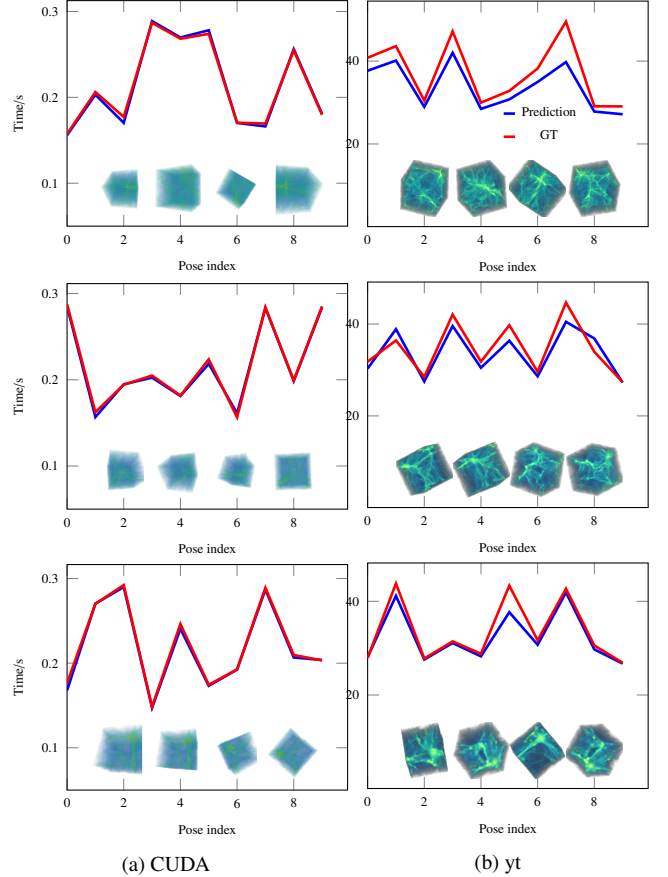


Figure 8: ENTIRE prediction and measured time (GT) for representative time steps of Nyx (248, 618, and 1080). The left and right column show results for the CUDA raycaster and yt, respectively.

t^{target} . The means to achieve this is by controlling the ray step size, δ , on the basis of predicted rendering time t^{pred} . As the basis for this, we experimentally determine a function $G(\cdot)$ that models the relative impact that ray step size has on rendering times. This is done by sampling rendering times of different volumes from different poses first, and normalizing them with respect to what is achieved with reference step size δ^{ref} (otherwise used throughout this work); this yields t^{norm} . Finally, we take the median value of all measured $G(\cdot)$ as our final function for ray step size adaption (implementation-wise, we store it as a lookup table and access it via linear interpolation).

With this, controlling the step size for each frame works as presented in algorithm 1: for each *pose* along the path, obtain a timing prediction from ENTIRE (which can be done in less than 0.3 ms as discussed above), and then using G we determine what adjustment to make from δ^{ref} to δ^{adapt} to eventually yield the target rendering timing when rendering.

The experiments in this use case employ the CUDA raycaster and MAESTROeX, from which we consider time steps 500, 1000, and 1500. Our exploration sequence lasts for 60s with a target rendering time of 100ms (corresponding to 10fps). In the sequence, the camera orbits the volume at a fixed distance to it with linearly varying spherical coordinates with respect to t . The poses for obtaining $G(\cdot)$ are presented in Figure 10. In Figure 11(a), we present all measured curves and G , the curve for the final ray step size adaption. Note that all curves behave in a similar pattern relatively

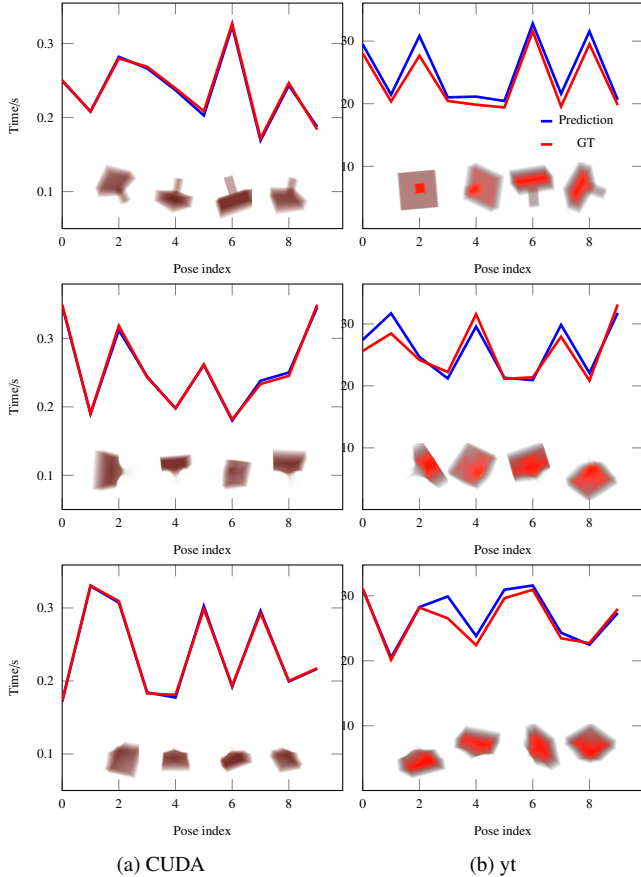


Figure 9: ENTIRE prediction and measured time (GT) for representative time steps of Pool (17, 110, and 203). The left column shows the CUDA raycaster, while the right column depicts yt.

speaking, even though their corresponding absolute timings differ.

The results for ray step size steering on this basis are presented in Figure 12. It can clearly be seen that with our adaptation of ray step size the achieved rendering time remains close to the target rendering time. Note that the achieved timing is generally a little shorter than the target, which can be attributed to the fact that G is practically stored as lookup table and accessed via linear interpolation (see Figure 11(b)). $\delta_{\text{pred}}^{\text{adapt}}$ is always slightly larger than $\delta_{\text{GT}}^{\text{adapt}}$ due to the shape of the curve, and consequently, the resulting rendering process is faster. This could be adjusted with an adapted interpolation scheme taking into account knowledge about the general shape of the curve. Nevertheless, our conservative adaptation could be considered to be desirable behavior in most application scenarios.

6.2 Load Balancing

We now discuss a distributed volume rendering use case with the CUDA renderer and the Nyx dataset. In this use case, we generate a database of images comprising 6 time steps and 64 poses (from a camera orbit), i.e., in total there are $6 \times 64 = 384$ visualization tasks. The goal is to distribute these rendering tasks across $\|N\|$ (identical) machines such that the maximum completion time across all machines (or nodes) $n \in N$ is minimized (whereas an optimal assignment typically also yields an evenly balanced load). Mathematically speaking, the objective is to determine an assignment

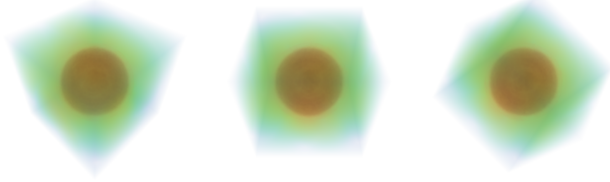


Figure 10: Three poses for obtaining $G(\cdot)$.

Table 6: Comparison of prediction accuracy (MSE in $\times 10^{-5}$ for the CUDA raycaster, $\times 10^0$ for yt) and inference time (in milliseconds per pose on average). “avgRT” provides average rendering time in ms. The best prediction results are highlighted in bold.

Framework	Dataset	avgRT	ENTIRE		[7]
			MSE \downarrow / $T_{\text{infer}}^{\text{vol}}$	\downarrow / $T_{\text{infer}}^{\text{pred}}$	MSE \downarrow / $T_{\text{infer}}^{\text{baseline}}$
CUDA raycaster	MAESTROeX	209.5	1.807/1.758/0.289		$403.5/6.284 \times 10^6$
	Nyx	211.5	1.317/1.853/0.285		$191.5/1.142 \times 10^7$
	Pool	242.7	1.852/1.781/0.293		$298.6/8.735 \times 10^6$
yt	MAESTROeX	33334.8	8.748/3.591/0.296		$389.6/9.937 \times 10^8$
	Nyx	25961.9	9.581/1.926/0.294		$211.4/1.799 \times 10^9$
	Pool	33124.3	2.200/2.301/0.291		$242.7/9.171 \times 10^8$

$A : N \rightarrow V$ of nodes N to visualization tasks V such that

$$\min_{A: N \rightarrow V} \left(\max_{n \in N} \left(\sum_{v \in A(n)} t(v) \right) \right), \quad (7)$$

where $t : v \rightarrow \mathbb{R}$ gives an assessment of anticipated rendering time of $v \in V$.

This problem is NP-hard even when assuming identical machines as we do here. To solve it, we employ LPT (Longest-processing-time-first), a greedy algorithm with a tight error bound [14]. LPT considers rendering tasks from high to low cost—here based on the timing predictions $t(\cdot)$ —and iteratively assigns them to nodes such that after each step the maximum cost across all nodes is minimal.

We compare three variants determining the time assessment $t(\cdot)$ used in Equation 7:

GT. Measured rendering times, i.e., assuming perfect predictions.

ENTIRE. The rendering times as estimated by ENTIRE.

Constant. All timings are assumed to be the same.

Note that with Constant the tasks are considered in random order by LPT, and the assignment yields a balanced task count.

Figure 13 shows the achieved results for a varying number of nodes $\|N\|$. The timings are normalized relative to the timing of the slowest node when scheduling with perfect (GT) prediction (i.e., relative to the outcome of Equation 7). Three boxplots are presented for each node count $\|N\|$, corresponding to GT, ENTIRE and Constant, respectively. They show the distribution of total rendering times $\sum_{v \in A(n)} t(v)$ across nodes $n \in N$. It can be seen that with higher node counts also the relative load imbalance increases for ENTIRE and Constant, while an even distribution is achieved throughout with GT. However, the high accuracy of ENTIRE allows LPT to distribute the load such that load imbalance—the range from the fastest to the slowest node—is smaller than 10% even for large $\|N\|$, whereas it is more than triple than that for Constant in comparison.

The three curves drawn over the boxplots in Figure 13 depict the maximum render time for each variant (it directly reflects the objective value to be minimized in Equation 7). The relative difference to the GT solution increases with $\|N\|$ for both ENTIRE and

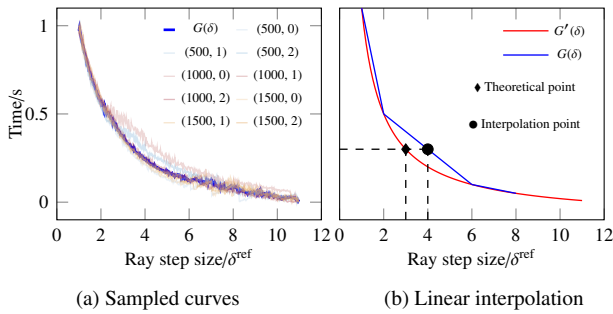


Figure 11: Our proposed ray step size adaption method. (a) Sampled δ - t^{norm} curves. Time step and pose index pairs are denoted in the form of (time step, pose index) in the legend. (b) Linear interpolation on $G(\delta)$; G' depicts the theoretical GT curve.

Constant. However, the results clearly demonstrate that, even with a high number of nodes, ENTIRE incurs less than a 4% additional cost compared to the GT, whereas Constant shows a significantly higher overhead, approaching 20%.

Overall, this demonstrates the potential of ENTIRE to save a significant amount of compute resources in larger-scale volume visualization setups, closely approximating the results of the theoretical optimum with perfect predictions.

7 CONCLUSION AND FUTURE WORK

Conclusion. We presented ENTIRE, a novel ML-based approach for predicting volume rendering time that does not require manually adjusting for the concrete method, hardware, or dataset used. Our approach comprises two-stages: (1) encoding the volume as a feature vector (VolumeNet), and (2) using this together with the camera configuration to predict rendering time (PredNet). We demonstrated that he proposed model achieves both high accuracy and inference speed across datasets, compute hardware, and methods, and showcased its utility in two scenarios: for steering computational cost by adapting rendering parameters and for balancing load in distributed scenarios.

Future Work. Subsequent volumes of time series typically exhibit a high degree of similarity, eventually resulting in redundancy in our training dataset. We plan to consider time step selection algorithms as a promising direction to address this (e.g., [13, 31]). Currently, VolumeNet and PredNet are trained separately and we aim to further investigate possibilities for joint training. While this can potentially further improve results, we also anticipate that this will pose difficulties in the training process, especially due to increased memory consumption. In addition, ENTIRE employs downsampling prior to VolumeNet to (mainly) improve training efficiency, which however potentially loses some finer details with high-frequency data and/or transfer functions. We aim to investigate ways to address this. Finally, we would like to further explore the potential of recently proposed autoencoder architectures to improve the volume’s feature representation in VolumeNet. For example, Kaiming *et al.* [16] demonstrated promising results with an asymmetric autoencoder (with reduced decoder size) trained on randomly masked images.

ACKNOWLEDGMENTS

We thank the Center for Information Technology of the University of Groningen for their support and for providing access to the Hábrók high performance computing cluster. We also thank the Deutsche Forschungsgemeinschaft (DFG, German Research Foundation) for supporting this work by funding SFB 1313 (Project Number 327154368).

REFERENCES

- [1] J. Ahrens, S. Jourdain, P. O’Leary, J. Patchett, D. H. Rogers, and M. Petersen. An image-based approach to extreme scale in situ visualization and analysis. In *SC’14: Proceedings of the International Conference for High Performance Computing, Networking, Storage and Analysis*, pp. 424–434. IEEE, 2014. 1, 4
- [2] A. S. Almgren, J. B. Bell, M. J. Lijewski, Z. Lukić, and E. Van Andel. Nyx: A massively parallel amr code for computational cosmology. *The Astrophysical Journal*, 765(1):39, 2013. 5
- [3] S. S. Bagsorkhi, M. Delahaye, S. J. Patel, W. D. Gropp, and W.-m. W. Hwu. An adaptive performance modeling tool for GPU architectures. In *Proceedings of the 15th ACM SIGPLAN symposium on Principles and practice of parallel programming*, pp. 105–114, 2010. 3
- [4] J. Beyer, M. Hadwiger, and H. Pfister. State-of-the-art in GPU-based large-scale volume visualization. In *Computer Graphics Forum*, vol. 34, pp. 13–37. Wiley Online Library, 2015. 1
- [5] V. Bruder, S. Frey, and T. Ertl. Real-time performance prediction and tuning for interactive volume raycasting. In *SIGGRAPH ASIA 2016 Symposium on Visualization*, pp. 1–8, 2016. 1, 3
- [6] V. Bruder, S. Frey, and T. Ertl. Prediction-based load balancing and resolution tuning for interactive volume raycasting. *Visual Informatics*, 1(2):106–117, June 2017. 1
- [7] V. Bruder, M. Larsen, T. Ertl, H. Childs, and S. Frey. A hybrid in situ approach for cost efficient image database generation. *IEEE Transactions on Visualization and Computer Graphics*, 2022. 1, 2, 3, 5, 7, 9
- [8] V. Bruder, C. Müller, S. Frey, and T. Ertl. On evaluating runtime performance of interactive visualizations. *IEEE transactions on visualization and computer graphics*, 26(9):2848–2862, 2019. 1, 3, 5
- [9] J. Chibane, T. Alldieck, and G. Pons-Moll. Implicit functions in feature space for 3d shape reconstruction and completion. In *Proceedings of the IEEE/CVF conference on computer vision and pattern recognition*, pp. 6970–6981, 2020. 2
- [10] J. Dayal, D. Bratcher, G. Eisenhauer, K. Schwan, M. Wolf, X. Zhang, H. Abbasi, S. Klasky, and N. Podhorszki. Flexpath: Type-based publish/subscribe system for large-scale science analytics. In *2014 14th IEEE/ACM International Symposium on Cluster, Cloud and Grid Computing*, pp. 246–255. IEEE, 2014. 2
- [11] A. Doi and A. Koide. An efficient method of triangulating equi-valued surfaces by using tetrahedral cells. *IEICE TRANSACTIONS on Information and Systems*, 74(1):214–224, 1991. 2
- [12] D. Fan, A. Nonaka, A. S. Almgren, A. Harpole, and M. Zingale. Mastrox: A massively parallel low mach number astrophysical solver. *The Astrophysical Journal*, 887(2):212, 2019. 5
- [13] S. Frey and T. Ertl. Flow-based temporal selection for interactive volume visualization. In *Computer Graphics Forum*, vol. 36, pp. 153–165, 2017. 2, 10
- [14] R. L. Graham. Bounds on multiprocessing timing anomalies. *SIAM Journal on Applied Mathematics*, 17(2):416–429, 1969. 9
- [15] P. Grosset and J. Ahrens. Lightweight interface for in situ analysis and visualization of particle data. In *ISAV’21: In Situ Infrastructures for Enabling Extreme-Scale Analysis and Visualization*, pp. 12–17. 2021. 2
- [16] K. He, X. Chen, S. Xie, Y. Li, P. Dollár, and R. Girshick. Masked autoencoders are scalable vision learners. In *Proceedings of the IEEE/CVF Conference on Computer Vision and Pattern Recognition*, pp. 16000–16009, 2022. 10
- [17] E. Ipek, B. R. De Supinski, M. Schulz, and S. A. McKee. An approach to performance prediction for parallel applications. In *Euro-Par 2005 Parallel Processing: 11th International Euro-Par Conference, Lisbon, Portugal, August 30-September 2, 2005. Proceedings 11*, pp. 196–205. Springer, 2005. 2
- [18] D. Kingma and J. Ba. Adam: A method for stochastic optimization. In *International Conference on Learning Representations (ICLR)*. San Diego, CA, USA, 2015. 5
- [19] G. Klambauer, T. Unterthiner, A. Mayr, and S. Hochreiter. Self-normalizing neural networks. *Advances in neural information processing systems*, 30, 2017. 3
- [20] M. Larsen, C. Harrison, J. Kress, D. Pugmire, J. S. Meredith, and

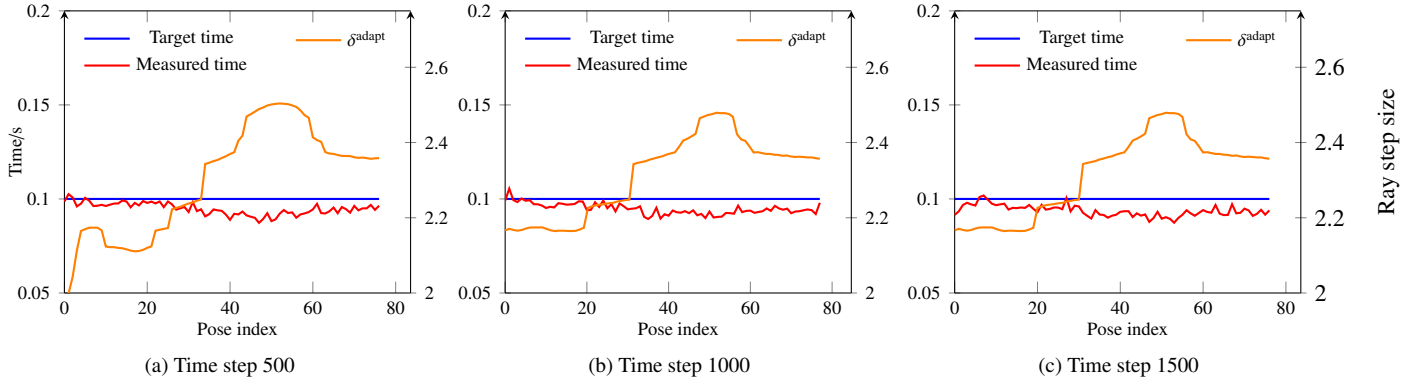


Figure 12: Adapted ray step size δ^{adapt} and rendering times for time steps 500, 1000, and 1500.

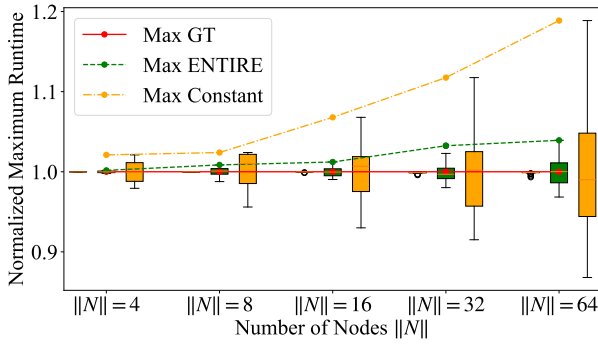


Figure 13: Load balancing use case. Boxplots show the distribution of total rendering times ($\sum_{v \in A(n)} t(v)$) across nodes $n \in N$. Lines highlight the maximum render time that determines the runtime until completion of all tasks. All timings are normalized with respect to the GT runtime.

H. Childs. Performance modeling of in situ rendering. In *Proceedings of the International Conference for High Performance Computing, Networking, Storage and Analysis*, pp. 1–12, 2016. 1, 3

[21] Y. Le Cun and F. Fogelman-Soulié. Modèles connexionnistes de l’apprentissage. *Intelligence*, 2(1):114–143, 1987. 2

[22] B. C. Lee, D. M. Brooks, B. R. de Supinski, M. Schulz, K. Singh, and S. A. McKee. Methods of inference and learning for performance modeling of parallel applications. In *Proceedings of the 12th ACM SIGPLAN symposium on Principles and practice of parallel programming*, pp. 249–258, 2007. 3

[23] W. E. Lorensen and H. E. Cline. Marching cubes: A high resolution 3d surface construction algorithm. In *Seminal graphics: pioneering efforts that shaped the field*, pp. 347–353, 1998. 2

[24] I. Loshchilov and F. Hutter. SGDR: Stochastic gradient descent with warm restarts. In *International Conference on Learning Representations*, 2017. 5

[25] J. N. Martel, D. B. Lindell, C. Z. Lin, E. R. Chan, M. Monteiro, and G. Wetzstein. ACORN: adaptive coordinate networks for neural scene representation. *ACM Transactions on Graphics (TOG)*, 40(4):1–13, 2021. 2

[26] L. Mescheder, M. Oechsle, M. Niemeyer, S. Nowozin, and A. Geiger. Occupancy networks: Learning 3d reconstruction in function space. In *Proceedings of the IEEE/CVF conference on computer vision and pattern recognition*, pp. 4460–4470, 2019. 2

[27] B. Mildenhall, P. P. Srinivasan, M. Tancik, J. T. Barron, R. Ramamoorthi, and R. Ng. NeRF: Representing scenes as neural radiance fields for view synthesis. *Communications of the ACM*, 65(1):99–106, 2021. 2

[28] M. Niemeyer, L. Mescheder, M. Oechsle, and A. Geiger. Occupancy

flow: 4d reconstruction by learning particle dynamics. In *International Conference on Computer Vision*, Oct. 2019. 2

[29] NVIDIA. Cuda samples, 2024. Accessed: 2024-10-03. 5

[30] S. Peng, M. Niemeyer, L. Mescheder, M. Pollefeys, and A. Geiger. Convolutional occupancy networks. In *Computer Vision—ECCV 2020: 16th European Conference, Glasgow, UK, August 23–28, 2020, Proceedings, Part III 16*, pp. 523–540. Springer, 2020. 2

[31] W. P. Porter, Y. Xing, B. R. von Ohlen, J. Han, and C. Wang. A deep learning approach to selecting representative time steps for time-varying multivariate data. In *2019 IEEE Visualization Conference (VIS)*, pp. 1–5. IEEE, 2019. 10

[32] C. Reiser, S. Peng, Y. Liao, and A. Geiger. KiloNeRF: Speeding up neural radiance fields with thousands of tiny MLPs. In *Proceedings of the IEEE/CVF international conference on computer vision*, pp. 14335–14345, 2021. 2

[33] S. Rizzi, M. Hereld, J. Insley, M. E. Papka, T. Uram, and V. Vishwanath. Performance modeling of v13 volume rendering on GPU-based clusters. In *Proceedings of the 14th Eurographics Symposium on Parallel Graphics and Visualization*, pp. 65–72, 2014. 3

[34] S. D. Roth. Ray casting for modeling solids. *Computer graphics and image processing*, 18(2):109–144, 1982. 2

[35] V. Sitzmann, M. Zollhöfer, and G. Wetzstein. Scene representation networks: Continuous 3d-structure-aware neural scene representations. *Advances in Neural Information Processing Systems*, 32, 2019. 2

[36] S. Sodhi, J. Subhlok, and Q. Xu. Performance prediction with skeletons. *Cluster Computing*, 11:151–165, 2008. 2

[37] S. Stegmaier, M. Strengert, T. Klein, and T. Ertl. A simple and flexible volume rendering framework for graphics-hardware-based ray-casting. In *Fourth International Workshop on Volume Graphics, 2005.*, pp. 187–241, 2005. 3

[38] A. Tewari, O. Fried, J. Thies, V. Sitzmann, S. Lombardi, K. Sunkavalli, R. Martin-Brualla, T. Simon, J. Saragih, M. Nießner, et al. State of the art on neural rendering. In *Computer Graphics Forum*, vol. 39, pp. 701–727. Wiley Online Library, 2020. 2

[39] G. Tkachev, S. Frey, C. Müller, V. Bruder, and T. Ertl. Prediction of distributed volume visualization performance to support render hardware acquisition. In *EGPGV@ EuroVis*, pp. 11–20, 2017. 1, 3

[40] M. J. Turk, B. D. Smith, J. S. Oishi, S. Skory, S. W. Skillman, T. Abel, and M. L. Norman. yt: A multi-code analysis toolkit for astrophysical simulation data. *The Astrophysical Journal Supplement Series*, 192(1):9, 2010. 5

[41] K.-C. Wang, T.-H. Wei, N. Shareef, and H.-W. Shen. Ray-based exploration of large time-varying volume data using per-ray proxy distributions. *IEEE Transactions on Visualization and Computer Graphics*, 26(11):3299–3313, 2019. 2

[42] M. Wimmer and P. Wonka. Rendering time estimation for real-time rendering. In *Rendering Techniques*, pp. 118–129, 2003. 3

[43] G. Wu, J. L. Greathouse, A. Lyashevsky, N. Jayasena, and D. Chiou. GPGPU performance and power estimation using machine learning. In *2015 IEEE 21st international symposium on high performance*

- computer architecture (HPCA)*, pp. 564–576. IEEE, 2015. 3
- [44] Q. Wu, D. Bauer, Y. Chen, and K.-L. Ma. Hyperinr: A fast and predictive hypernetwork for implicit neural representations via knowledge distillation. *arXiv preprint arXiv:2304.04188*, 2023. 2
- [45] A. Yu, V. Ye, M. Tancik, and A. Kanazawa. pixelNeRF: Neural radiance fields from one or few images. In *Proceedings of the IEEE/CVF Conference on Computer Vision and Pattern Recognition*, pp. 4578–4587, 2021. 2
- [46] Y. Zhang and J. D. Owens. A quantitative performance analysis model for GPU architectures. In *2011 IEEE 17th international symposium on high performance computer architecture*, pp. 382–393. IEEE, 2011. 3